In: Cyclones: Formation, Triggers and Control
Editors: K. Oouchi and H. Fudeyasu
ISBN: 978-1-61942-976-5

Chapter 6

ESTIMATION OF CHANGES IN TROPICAL CYCLONE INTENSITIES AND ASSOCIATED PRECIPITATION EXTREMES DUE TO ANTHROPOGENIC CLIMATE CHANGE

Junichi Tsutsui*
Central Research Institute of Electric Power Industry, Japan

Abstract

On the basis of theoretical models for the maximum potential intensity of tropical cyclones and general precipitation extremes, a simple scheme has been developed to estimate climatological changes in tropical cyclone intensities and associated precipitation extremes as a function of global surface temperature anomalies caused by anthropogenic climate changes. Since intensity changes strongly depend on the upper-air warming relative to the surface, this scheme incorporates the uncertainty of the variation in the upper-air temperature anomalies obtained from multiple-climate model experiments. A case study of Typhoon Flo in 1990 right before its landfall in Japan has revealed that its intensity, measured by a central pressure drop at sea level, and peak precipitation are projected to increase by 6.5% and 9.3%, respectively, under a globally 1-°C warmed environment relative to the present. These quantities and associated wind speed changes are directly calculated with uncertainties for arbitrary warming anomalies, which enables quantitative assessment for a wide range of greenhouse-gas emissions pathways in the future.

1. Introduction

The tropical cyclone (TC) is one of the most devastating atmospheric phenomena. To adequately prepare for their strong winds and torrential rains, societies affected by TCs require adequate preparation measures that include disaster prevention, appropriate infrastructure design, and water resource management. These measures can be adversely affected by socioeconomic circumstances in some regions and insufficient scientific understanding of

*E-mail address: tsutsui@criepi.denken.or.jp

TCs, in particular, the relationship between TC activity and natural climate variability and anthropogenic climate changes. This chapter considers the possible effects of long-term greenhouse gas-induced (GHG-induced) global warming on TC activity from a policymaker's perspective.

Recent modeling studies suggest an increase in intensity and a decrease in frequency of global TCs in warmed climates as summarized in the fourth assessment report (AR4) of the Intergovernmental Panel on Climate Change (IPCC) [1]. The intensity increase has a theoretical basis [2–4], and is believed to be relatively confident. Prospects for this trend have been discussed in a more recent review [5]. Global TC tendencies, however, are not necessarily the same as regional TC tendencies, which depend on large-scale circulations and spatial distributions of thermodynamic conditions in the tropics [6, 7]. Although different regional TC tendencies in numerical experiments appear to be explained by the modulation of natural climate variability [8], currently used atmosphere-ocean general circulation models (AOGCMs) cannot predict consistent trends in mean states and variability in the tropics [9, 10]. Moreover, fundamental challenges are encountered in deducing long-term regional tendencies from past observations; the duration of reliable and consistent TC records is too short to find any anthropogenic changes from relatively large fluctuations relevant to natural variations with different time scales [11]. Thus, at the current stage of scientific understanding, it is difficult to quantify the warming impact on all aspects of TC activity in a specific region.

From a policymaker's perspective, improvements to guard against possible TC intensification are rational, regardless of global warming impacts on TC activity [12]. Motivated by a growing need for appropriate adaptation to the warming environment, the author has applied a maximum potential intensity (MPI) theory to TCs in the western North Pacific, considering the uncertainty of thermodynamic conditions obtained through various AOGCMs [13]. Although the information from this study is limited to changes in the MPI, i.e., the maximum intensity of an idealized TC, this theory is a key aspect of risk management for avoiding complexities and uncertainties associated with the frequencies and motions of regional TCs. On the basis of this study and subsequent one [14], the present chapter provides a scheme to quantify changes in TC-caused strong winds and torrential rains prevalent in warmed climates.

As documented in Reference [15], TC-caused torrential rains involve complex physical processes relevant to water vapor supply and atmospheric instability in conjunction with embedded mesoscale circulation systems, orographic effects, and interactions with large-scale circulations including mid-latitude synoptic systems. Although these issues should be investigated from intensive observations and numerical experiments for better forecast and understanding of their mechanisms, a simple physically-based method has an advantage in quantifying GHG-induced background changes. Therefore, we employ a simple formula to assess changes in precipitation extremes from large-scale conditions resolved by AOGCMs [16].

The present scheme to estimate changes in the MPI and precipitation extremes can be formulated as a function of the global surface temperature anomaly by using appropriate pattern scaling to derive regional anomalies in thermodynamic conditions. This formulation is useful for risk assessment because it considers various types of uncertainties in a hierarchical structure. Moreover, planning adaptation to possible TC intensification depends

on mitigation policies to reduce GHG emissions, which involves considerable uncertainties of climate sensitivity [17] and socio-economic development pathways. Since the global temperature anomaly is a common variable for both mitigation and adaptation studies, the formulation presented in this chapter is applicable to an integrated research framework for examination of mitigation and adaptation strategies, which leads to activation of rational plans and evaluation of priorities.

In a case study contained in this chapter, large-scale conditions used in calculating MPI and precipitation extremes in the present and future warmed climates were obtained from the JRA-25 long-term reanalysis of the global atmosphere [18] and recent multiple AOGCM experiments conducted in the framework of the Coupled Model Intercomparison Project phase 3 (CMIP3) [19]. The JRA-25 is one of the long-term reanalyses and has an advantage of better quality of precipitation analysis in the tropics [20]. The CMIP3 has formed the basis of the AR4 and is used here to derive regional anomalies in thermodynamic conditions. These datasets should be substituted by more advanced ones when available.

In the rest of this chapter, the methodology on the basis of the MPI theory is described in Section 2; a case study is presented and discussed in Section 3; and the summary and remaining issues are stated in Section 4.

2. Methodology

2.1. MPI theory

As distinct from an extratropical cyclone, the TC has a circularly symmetric warm-core structure. The warm core is formed by the release of latent heat in the upper air through convection originating from moist surface air. Upper air that is warmed directly reduces surface pressure to maintain the hydrostatic balance, and surface pressure drops over the warm sea surface to increase substantially the moist entropy, which accelerates upper air warming. This interaction between upper air warming and an increase in surface moist entropy is essential for TC development, where the surface temperature and water vapor amount are important factors in determining the upper boundary of the drop in surface pressure and the associated maximum wind speed, referred to as the MPI.

Two different MPI theories have been provided by Emanuel [2,3] and Holland [4]. The former considers the energy balance between the heat transfer from the ocean and the frictional dissipation at the surface to derive the MPI of a steady-state developed TC in terms of maximum surface wind. Available energy acquired from the ocean is formulated using an analogy with a Carnot cycle heat engine with the efficiency expressed by the temperature difference between the surface and the top of the storm. Meanwhile, Holland's theory considers thermodynamic processes in the inner core of a developing TC to calculate the upper-air warming associated with moist-adiabatic updraft in the eyewall and dry subsidence in the eye, leading to a reduction in the surface pressure. Although these theories have limitations in forecasting the intensity of individual TCs [21, 22], they can provide basic information on climatological MPI to reflect global changes in thermodynamic environments including different upper-air warming anomalies [7, 23–25].

A tropical atmosphere characteristic is the presence of warming anomalies amplified toward the upper troposphere, originating from the moist adiabatic ascent of convective

air parcels [26]. TC intensification due to an increase in surface temperature is generally suppressed to some extent by greater upper-air warming in the environment, the degree of which is one of the major variables in climatological MPI in warmed climates. Here, we employ Holland's theory because it directly accounts for the warming structure and its variations in a simple manner. In this regard a care is needed because Holland's MPI appears to be more sensitive to global warming than Emanuel's MPI [5].

Essentially, Holland's MPI is expressed by the central pressure at sea level p_c and evaluated through the hydrostatic balance

$$\delta p_c = \frac{p_s}{T_v(p_s)} \int_{p_s}^{p_t} \delta T_v d \ln p, \tag{1}$$

where δp_c is the sea-level pressure drop, defined as the pressure difference between the environment and the TC center; p is the pressure; p_s is the surface pressure; p_t is the pressure at the top of the TC, and changes are negligible above it; T_v is the virtual temperature; and δT_v is its deviation from the environment.

The deviation of temperatures in the inner-core of a developing TC is determined for a given sea surface temperature (SST) and an upper-air temperature profile in the environment by calculating a moist-adiabatic ascent in the eyewall under isothermal conditions at the surface and dry subsidence in the eye. The surface relative humidity (RH) beneath the eyewall and the RH profile in the eye are assumed appropriately such that the maximum δp_c for the present climate becomes consistent with empirical findings. Computing implementation and sensitivity to key parameters are given in Reference [13].

The amount of water vapor providing latent heat increases with warmer SSTs, and the δT_v increases with cooler upper-air temperatures in the environment. The δp_c, therefore, increases with warmer SST and cooler upper-air temperatures in the environment. The calculation of the MPI does not consider SST cooling by TC-induced ocean upwelling and dynamic conditions in the atmosphere that suppress TC development. Although real TCs do not necessarily attain their MPI due to these restrictions, the climatological MPI constrains well the minimum central pressures of individual TCs, as illustrated in Fig. 1. Realized central pressures are more scattered at lower latitudes and more confined at higher latitudes, which is consistent with temporal and latitudinal MPI variations. This consistency ensures climatological use of the MPI.

It should be noted that some realized pressures exceed a suggested lower limit by the MPI, which is partly due to the incomplete spatial representation of the MPI for northward-moving TCs. Namely, it is possible that the intensity of such a TC was resulted from warmer conditions at lower latitudes that it had experienced previously. Conversely, realized pressures generally do not reach a suggested lower limit at lower latitudes from June to July, which implies that TC development in the early season is more constrained by the dynamic conditions of large-scale circulations.

2.2. Wind speed scaling

Wind velocities in a TC can be approximated by axisymmetric gradient winds. The gradient wind balance in cylindrical coordinates (r, θ, z) is given by

$$\frac{v_\theta^2}{r} + f v_\theta = \frac{1}{\rho} \frac{\partial p}{\partial r}, \tag{2}$$

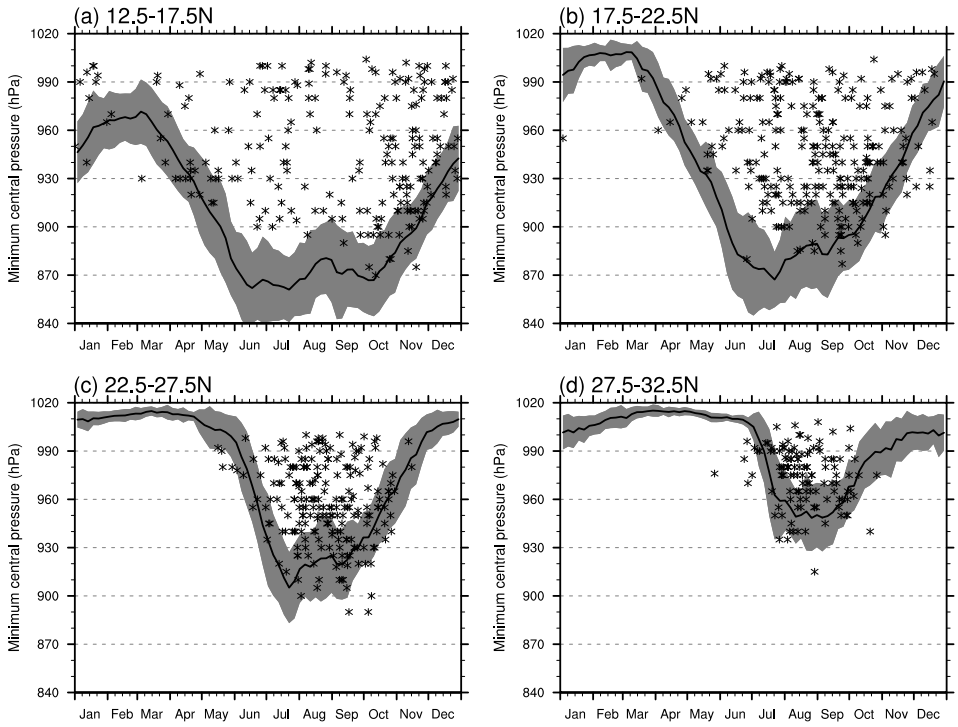

Figure 1. Climatological annual cycles of MPI in the western North Pacific region 12.5°N–32.5°N, 122.5°E–145°E, compared with minimum central pressures of individual TCs from the JMA best track during 1951–2009. Shading indicates plus/minus one standard deviation of interannual variability. The region is divided into four latitude ranges: (a) 12.5°N–17.5°N, (b) 17.5°N–22.5°N, (c) 22.5°N–27.5°N, (d) 27.5°N–32.5°N. Each individual TC is marked in one of the four panels, depending on the region including the latitude at which the TC attained minimum pressure. Updated from Fig. A1 of Reference [13].

where v_θ is the tangential velocity (positive for anticlockwise flow), f is the Coriolis parameter, and ρ is the density of air. According to Reference [27], this equation is transformed into a relationship between the vertical gradient of the absolute angular momentum and the radial temperature gradient considering the hydrostatic balance:

$$\frac{1}{r^3}\frac{\partial M_\theta^2}{\partial z^*} = \frac{R}{H}\frac{\partial T}{\partial r}, \tag{3}$$

where M_θ is the absolute angular momentum defined as $v_\theta r + fr^2/2$, z^* is the vertical independent variable in log-pressure coordinates defined as $-H\log(p/p_s)$, R is the gas constant for dry air, and H is a standard scale height defined as $R\bar{T}/g$; $\bar{T}$ is the global average temperature and g is the magnitude of gravity.

In Holland's MPI theory, the pressure drop is estimated from the vertical integration of temperature deviations with respect to the logarithm of pressure as expressed by equation (1). Then, the rate of change in wind speed can be estimated from that of the pressure drop through equation (3). Specifically, by considering a warm-core wind structure and assuming $\partial M/\partial z^* \sim v_\theta r/H$, we can approximate a temperature deviation in the warm-core

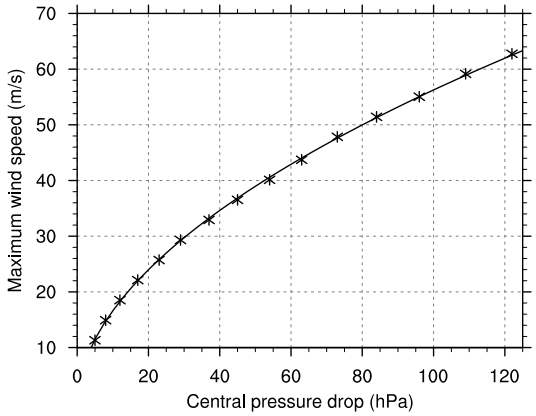

Figure 2. Relationship between the maximum surface (10-min) wind speeds and pressure drops at sea level of TCs in the western North Pacific. Asterisk markers represent values of the table used in the Japan Meteorological Agency [29], and the line is an approximate curve fitted to the values.

structure by integrating equation (3) with respect to r as

$$\delta T \sim \frac{UL}{R}\left(f + \frac{2U}{L}\right), \tag{4}$$

where U is the tangential velocity scale, which we regard as the maximum wind speed, and L is the horizontal scale of the warm-core structure. Assuming that the warmed climate does not change the horizontal scale of TCs, and considering an approximately proportional relationship between δT and δp_c in equation (1), we obtain

$$\frac{\Delta(\delta p_c)}{\delta p_c} = \left[1 + \frac{1}{1 + fL/(2U)}\right]\frac{\Delta U}{U}. \tag{5}$$

Since the Rossby number $U/(fL)$ is generally greater than unity for TCs, the term in the brackets [ ] in the previous equation is estimated to be slightly less than 2, and it turns out that the rate of change in wind speed is related to the rate of change in δp_c by a factor slightly greater than 0.5.

This factor can be determined from an empirical wind-pressure relation of TCs. According to Reference [28], one such empirical formula is given as

$$v_s = a(\delta p_c)^b, \tag{6}$$

where v_s is the surface maximum wind speed, and parameters a and b are determined, for example, as 4.9 and 0.53, respectively, by fitting this equation to the wind-pressure table used in the operational TC analysis at the Japan Meteorological Agency (JMA) [29], as shown in Fig. 2. v_s is defined as 10-min sustained wind at the reference (10 m) height, and the exponent 0.53 corresponds to the ratio of the rate of change in wind speed to the rate of change in the pressure drop.

When surface pressures in a TC are specified, the gradient wind balance gives an idealized wind profile from the center to the outside environment [30]. One widely used empirical representation uses pressure as an inverse exponential function of radius [31]

$$p_s = p_c + \delta p_c \exp\left(-\frac{r_m}{r}\right), \tag{7}$$

where r_m is the radius of maximum wind. By using this equation and the relationship between the curvature radius of the streamlines R_s and the trajectories R_t [27]

$$R_s = R_t\left(1 - \frac{V_c \cos\gamma}{v_\theta}\right), \tag{8}$$

the gradient wind associated with a moving TC is obtained as

$$v_\theta = \frac{fr - V_c\cos\gamma}{2}\left[-1 + \sqrt{1 + \frac{4rG}{(fr - V_c\cos\gamma)^2}}\right], \tag{9}$$

$$G = \frac{1}{\rho}\delta p_c \frac{r_m}{r^2}\exp\left(-\frac{r_m}{r}\right), \tag{10}$$

where V_c is the speed of TC motion, γ is the angle between the streamlines (in this case, pressure contours) and the direction of TC motion, and G is the pressure gradient force. In this derivation, the r in the first term in the left-hand side of equation (2) (centrifugal force) is replaced with R_t. This wind profile is conventionally used for engineering applications [32].

Figure 3 shows an example of wind distribution, where the parameters are roughly adjusted for the specific TC described in the next section. The component of non-axisymmetric winds is relatively large near the center, and the maximum wind occurs at the right of the TC motion, as empirically known. This idealized wind distribution, however, differs from winds in an actual TC such that the winds in the outer circulation often vary independently of the vortex core [30]. Moreover, the winds associated with a TC moving into middle latitudes, such as that illustrated by this example, are modified by its transition to an extratropical system [33]. Nevertheless, the idealized distribution is useful for quantifying background changes created by warmed climates.

Figure 3 illustrates the rate of change in the wind speed relative to that in the δp_c. The value is 0.5–0.6 in the core region including the radius of maximum wind and increases toward the outer region. The factor of 0.53 is appropriate for the maximum wind. When scaling wind speed change by the δp_c change, however, this value should be larger for the winds in a remote region that may affect wind-induced waves and storm surges.

2.3. Precipitation extreme

Precipitation rates associated with severe events are expected to increase in warmed climates because atmospheric water vapor amounts increase in these conditions. Assuming that the water vapor is saturated when a severe event occurs, one can evaluate the rate of change in the precipitation rate with respect to warming according to a well-known relationship between temperature and saturation water vapor pressure. Here, we relate a change in

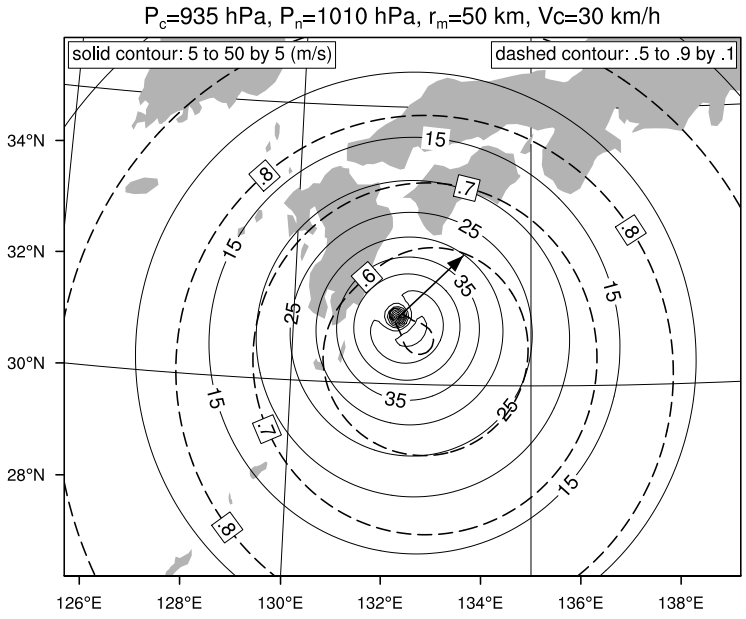

Figure 3. Example of the gradient wind distribution associated with a moving TC: p_c=935 hPa, δp_c=75 hPa, r_m=50 km, V_c=30 km h^{-1} (northeastward). Solid contours show the gradient wind speeds, and dashed contours show the ratios of the fractional change in the wind speed to that in the δp_c.

a peak precipitation rate associated with a TC to a change in the MPI by using the method provided in Reference [16]. This method is a more rational approach to warming impact because it considers changes in updraft profile in addition to the amount of water vapor.

When a severe precipitation event occurs, the rate of water vapor condensation with respect to time in the upper atmosphere is given by

$$c = -\omega \left. \frac{dq_s}{dp} \right|_{\theta^*}, \tag{11}$$

where ω is the pressure velocity, q_s is the saturation specific humidity, and the derivative of q_s with respect to p is evaluated along a constant equivalent potential temperature, denoted by θ^*. In this equation, the condensation rate is determined such that the rising air maintains the saturation amount of water vapor.

The precipitation rate is expressed as mass-weighted vertical integration of equation (12) and given by

$$P_e = -\left\{ \omega_e \left. \frac{dq_s}{dp} \right|_{\theta^*, T_e} \right\}, \tag{12}$$

where P_e is the precipitation extreme, defined as a high percentile of precipitation rate; ω_e is the corresponding vertical velocity; T_e is the corresponding temperature at which the θ^* is evaluated; and the braces $\{\ \}$ denote a mass-weighted vertical integration. In our scheme, the precipitation extreme and MPI are calculated for given climate conditions obtained from datasets of the global atmospheric reanalysis and AOGCM experiments. Since these climate conditions are represented by a coarse horizontal resolution, typically 100–300 km,

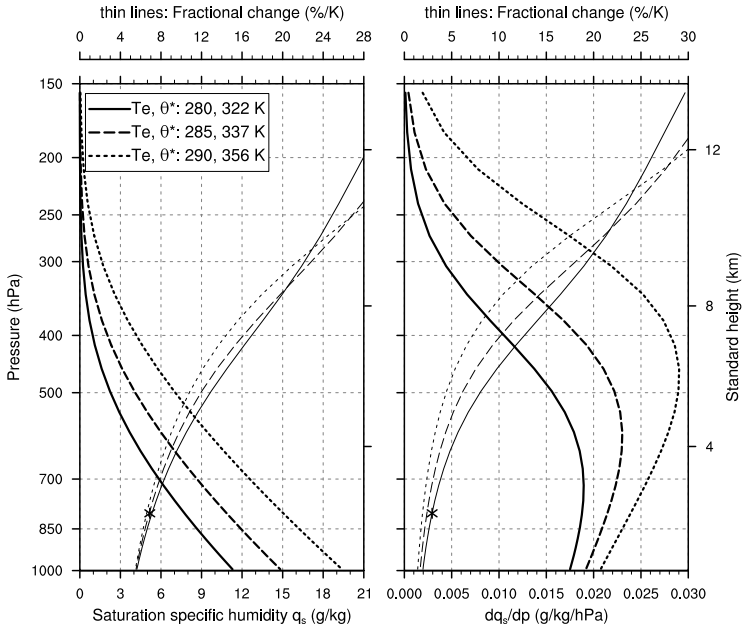

Figure 4. Profiles of saturated specific humidity q_s (left panel) and its vertical derivative $(dq_s)/(dp)|_{\theta*}$ (right panel) for three reference temperatures at the 800 hPa level. The rate of change in these quantities with respect to the reference temperature is indicated by thin lines with the upper auxiliary horizontal axis. The asterisk markers indicate the rate of change at the 800 hPa level for the reference temperature of 280 K, which are $6.9\%\,\mathrm{K}^{-1}$ and $2.9\%\,\mathrm{K}^{-1}$ for q_s and $(dq_s)/(dp)|_{\theta*}$, respectively.

we regard the variables in equation (12) as that of model-grid scale, whereby small-scale variations such as a convective downdraft and re-evaporation of condensated water vapor are implicitly included.

Here, we define the T_e as a temperature at the 800 hPa level. This level corresponds to about 2 km of standard atmosphere altitude, and is close to the level at which the amount of atmospheric water vapor is vertically divided into two equal amounts. As shown in Fig. 4, while the rate of change in q_s with respect to T_e is relatively large in the upper troposphere, that in the lower troposphere including a larger amount of water vapor is small, typically $7\%\,\mathrm{K}^{-1}$ at 800 hPa. With regard to precipitable water, defined as mass-weighted vertical integration of q_s, the rate of change is about $8\%\,\mathrm{K}^{-1}$. In contrast, the rate of change in dq_s/dp is significantly small in the lower troposphere, typically $3\%\,\mathrm{K}^{-1}$. An increase in precipitation extremes due to warming is, therefore, not as large as that inferred from the rate of change in specific humidity. In the case of a severe disturbance such as a TC reaching the tropopause, however, the rate of change becomes larger than $3\%\,\mathrm{K}^{-1}$, as determined from the rate of change in dq_s/dp, which is amplified at upper levels.

When estimating the P_e for a specific TC event, the ω_e and T_e can be specified according to the peak precipitation rate near the TC center. An increase in P_e due to climate warming is the result of two effects: a dynamic effect such that an intensified TC enhances water vapor transport, and a thermodynamic effect such that the amount of water vapor

increases in a warmed environment. In equation (12), changes in ω_e represent the former relevant to TC intensity, and changes in dq_s/dp that depends on T_e represent the latter. The dynamic effect can be related to MPI change, and the thermodynamic effect is calculated with consideration of the T_e anomaly, which will be demonstrated in a case study.

Since the ω_e is related to the maximum wind speed on the basis of the continuity equation, the ω_e in warmed climate can be scaled to that of the maximum wind speed. For simplicity, the rate of change in ω_e can be substituted with that of the maximum wind speed at all of the pressure levels with the assumption that the vertical structure of ω_e is not affected by the warming.

3. Case study

3.1. Typhoon Flo (1990)

In this chapter, we examine Typhoon Flo (1990), which brought excessive rainfall to Japan, as a case study to evaluate the aforementioned scheme to estimate changes in the pressure drop δp_c and the peak precipitation P_e for a given warmed environment. Although not explicitly described, changes in wind speed are scaled with those of δp_c. International field experiments were conducted in August–September 1990, which includes the life cycle of Flo [34]. It is believed that intensive observations in the field experiments were incorporated into the best track [1], shown in Fig. 5 (left), and the JRA-25 reanalysis of the global atmosphere.

Flo intensified rapidly with northwestward movement. Its minimum central pressure of 890 hPa was recorded at 0000 UTC on September 17 near Okinawa. The typhoon then recurved northeastward and made landfall in Wakayama Prefecture at about 2000 JST September 19 with a central pressure of 945 hPa. The JMA reported that the total rainfall over Japan throughout the event (September 12–13, 15, and 17–20), including rainfall due to the front affected by Flo, exceeded 1100 mm in parts of Shikoku and Kinki districts. According to the JMA's Automated Meteorological Data Acquisition System (AMeDAS), which includes about 1300 surface observation sites throughout Japan, daily rainfall during Flo's landfall on September 19 exceeded 100 mm at 230 sites with a maximum of 638 mm.

It is found from six-hourly reanalysis at about 1.1°-grid resolution that the rainfall associated with Flo peaked at 0000 UTC on September 19 just prior to landfall. Here, we focus on the typhoon's maximum updraft at that time and apply its pressure velocity profile as the ω_e for this event. As shown in Fig. 5 (right), the maximum updraft is located at 32.0N, 132.8E, south of Japan's main islands, and the upward motion is analyzed throughout the troposphere with its maximum at about 500 hPa. The peak precipitation rate of the reanalysis is 241 mm d^{-1}, which coincides with the maximum updraft, and is regarded as the peak precipitation (P_e) over the ocean without the orographic effect.

An increase in precipitation rates caused by the orographic effect of Japan's main islands can be estimated by using a factor of 2.5–3.0 according to a case study on Typhoon Owen in 1979 [35], the characteristics of which are similar to that of Flo. The AMeDAS

[1]The track data is taken from the RSMC (Regional Specialized Meteorological Center) Tokyo-Typhoon Center `http://www.jma.go.jp/jma/jma-eng/jma-center/rsmc-hp-pub-eg/trackarchives.html`

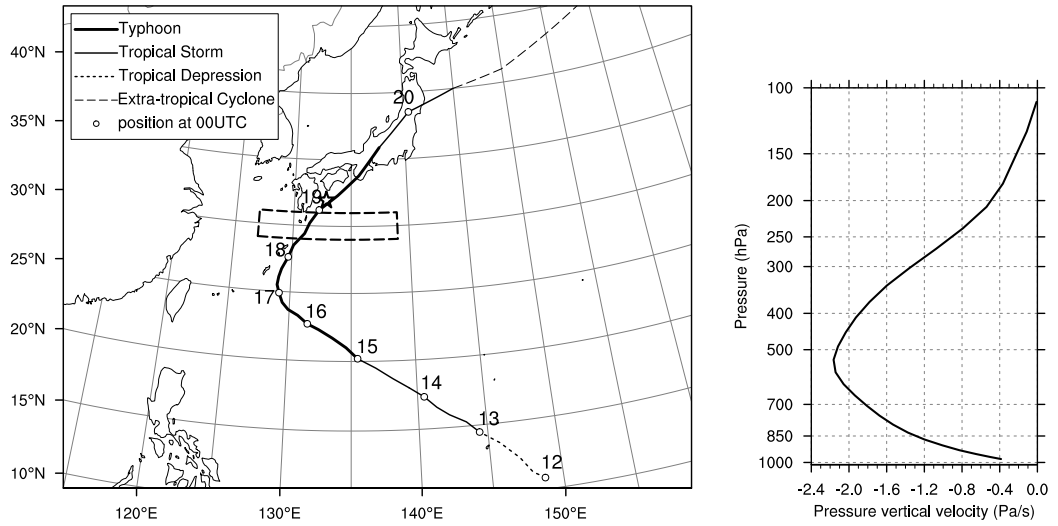

Figure 5. Track of Typhoon Flo and the vertical profile of the ω_e selected as the maximum updraft at 0000 UTC on September 19, 1990. The maximum updraft is located at 32.0°N, 132.8°E, indicated by the star marker on the map. The dashed rectangle on the map is the region of 29°N–31°N, 127°E–139°E, referred to for T_e and MPI calculation. Source: Figure 1 of Reference [14].

maximum of 638 mm is 2.6 times greater than the JRA-25 peak value of 241 mm, which is within the estimated range of the orographic effect.

The T_e in equation (12) is the temperature of the air parcel creating the updraft. Considering that a moist southerly caused Flo's torrential rains, we evaluate the T_e in the region of 29°N–31°N, 127°E–139°E (dashed rectangular in Fig. 5). The JRA-25 climatology (1979–2004 average) indicates an August–September mean temperature of 288.9 K in this region. By using this temperature as the T_e in addition to the ω_e profile, the P_e in equation (12) results in 260 mm d^{-1}. Despite ad hoc interpretation of T_e, this result is close to the peak value in the reanalysis, and the T_e value is acceptable as a base temperature in the present climate to assess changes due to warmed climate. Note that the rate of change in P_e in response to global warming, which will be shown subsequently, does not generally depend on the choice of T_e although the base value of P_e in the present climate is directly controlled by T_e.

For consistency, we use the same climatology for input data for MPI calculation (sea level pressure, SST, and upper-air temperatures). In this case, the SST is 28.3°C, which results in an MPI (δp_c) of 944 hPa (65 hPa) for the present climate. This MPI value is close to the observed central pressure at landfall, implying that Flo nearly attained the climatological MPI during the active TC season in the western North Pacific.

3.2. Pattern scaling of environmental changes

We need anomalies in sea surface and upper-air temperatures in the specified region to assess changes in the δp_c and P_e for a given anomaly in the global surface temperature

relative to the present climate, denoted as $\Delta\bar{T}_s$. Here, we employ the ensemble of the CMIP3 multi-model climate experiments to derive these anomalies by linear pattern scaling, which proportionally adjusts a given basic warming pattern to a $\Delta\bar{T}_s$. Although the regional climate change is not necessarily proportional to the $\Delta\bar{T}_s$, it has been proved that the general spatial pattern does not significantly depend on the degree of warming [1].

The basic warming pattern of the anomalies has been obtained from the ensemble means of 23 AOGCMs and is defined as 2080–99 climatology from the SRES [36] A1B run relative to the 1980–99 climatology from the historical run. The SRES A1B is one of three future scenarios used in the CMIP3, providing a "medium-warming" baseline projection for the AR4. Specifically, the basic pattern has been created as follows:

1. For the individual AOGCMs, create anomalies of surface and upper-air temperatures in monthly climatology.

2. For the surface temperatures, compute the ensemble means over all the AOGCMs and divide them by the global annual mean for normalization.

3. For the upper-air temperatures, divide the individual anomalies by the surface temperature anomaly at the same grid point for normalization, and then, compute the ensemble means of the normalized vertical profiles over all of the AOGCMs and two subsets of AOGCMs.

Here, we set aside uncertainties of surface anomaly patterns and climate sensitivity to focus instead on uncertainties of upper-air warming amplification that controls the degree of TC intensification due to the surface warming. This amplification depends on the model's formulation; particularly, its physics parameterizations. To quantify this uncertainty range, the two subsets of AOGCMs mentioned in step 3 of the above procedure have been selected such that they rank as the six largest or smallest anomalies at the 200-hPa level for each month and grid point. The ensemble means over all of the models provide the best estimate while those over the larger and smaller anomaly models represent warmed environments corresponding to suppressed and enhanced TC intensification, respectively.

In the August–September climatology of the specified region, the normalized surface temperature anomaly is 0.86, and the normalized upper-air temperature anomalies are obtained as shown in Fig. 6. The normalized anomaly at the 200-hPa level is 2.4 for all of the CMIP3 models while the values are 3.0 and 2.0 for the selected larger and smaller anomaly models, respectively. For a given $\Delta\bar{T}_s$, the value multiplied by 0.86 gives the SST anomaly in the region, and scaling the three profiles in Fig. 6 by this SST anomaly yields corresponding upper-air temperature anomalies.

Changes in the δp_c and P_e for a given $\Delta\bar{T}_s$ are obtained through the following procedures:

1. Estimate the regional temperature anomalies from a given $\Delta\bar{T}_s$ by using the pattern scaling.

2. Compute the fractional change of the δp_c from the MPI difference between the present and warmed climate.

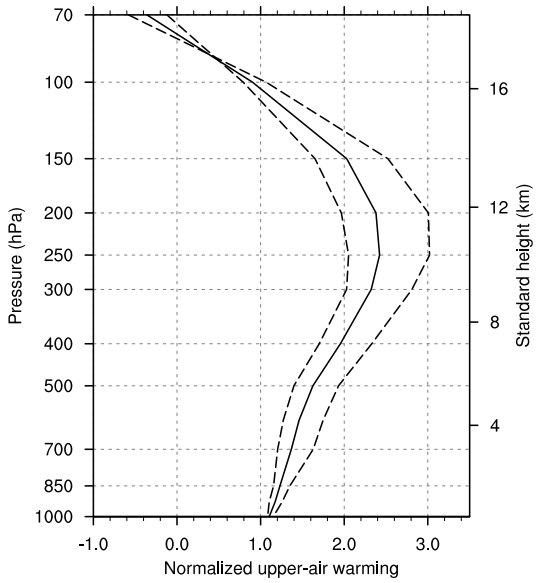

Figure 6. Normalized anomalies in August–September upper-air temperatures in the region of 29°N–31°N, 127°E–139°E. The solid line indicates ensemble means of all of the CMIP3 models, and each dashed line indicates those of subset models ranking as the six largest/smallest anomalies at the 200-hPa level. Source: Figure 2 of Reference [14].

3. Estimate the fractional change of the maximum wind speed near the TC center by using the ratio of the wind speed change to the δp_c change, which is typically 0.53.

4. Estimate the ω_e profile in the warmed climate by scaling that in the present climate in proportion to the maximum wind speed.

5. Compute the fractional change of the P_e from its difference between the present and warmed climate.

3.3. Representative changes

Table 1 summarizes results for the $\Delta\bar{T}_s$ of 1°C and 2°C. The rates of change in the δp_c and P_e for the 1°C warming are 6.5% and 9.3%, respectively, as the best estimates, which are nearly half that of the 2°C warming. The uncertainty of δp_c ranges from slightly less than the present level to almost twice that of the best estimate. This uncertainty range comes from the variations of the normalized temperature anomalies shown in Fig. 6, and the greater deviation of the normalized temperature anomalies for the larger anomaly models is responsible for the slight skewness of the uncertainty range.

The MPI change due to CMIP3 warming anomalies has been examined for broader applications to TC seasons and regions of development in the western North Pacific, where the average fractional change in the δp_c is 3.6%, 8.4%, and 19% in response to SST increases of 0.5, 1.0, and 2.0°C, respectively [13]. This relationship between TC intensification and SST increase is essentially comparable to representative studies based on observations [37]

Table 1. Fractional changes in the δp_c and P_e for Typhoon Flo just prior to landfall. Numbers in brackets are uncertainty ranges reflecting the variations of upper-air temperature anomalies. Numbers in the column denoted by P_e(*) are the fractional changes due to the thermodynamic effect alone (δp_c unchanged)

$\Delta\bar{T}_s$ (°C)	δp_c (%)	P_e (%)	P_e(*) (%)
1.0	6.5 [−1.6, 12.2]	9.3 [4.7, 12.4]	5.6
2.0	14.2 [−2.7, 26.1]	19.7 [9.8, 26.8]	11.3

and numerical simulations [25, 38]. The δp_c change of 6.5% for the 1°C warming (corresponding to 0.86°C SST rise) in the present case study also agrees with this TC basin-wide relation.

The fractional change in the P_e is larger than that in the δp_c, and the thermodynamic effect accounts for more than half of this P_e change. For the 1°C warming, the thermodynamic effect is 5.6%. This value, although greater than the typical value of 3% for the dq_s/dp in the lower troposphere, is less than the typical value of 7–8% for the q_s in the lower troposphere and the precipitable water. The uncertainty range for the P_e change is relatively small because it reflects the variation of the dynamic effect alone in the present scheme through the ω_e scaling. The thermodynamic effect is essentially believed to be robust.

The present scheme can be applied to assess secular changes in the δp_c and P_e for future scenarios. Here, we consider the representative concentration pathways (RCPs) [39] used as the common forcing data for climate projections toward the fifth assessment report of the IPCC, planned for publication in 2013–14. The RCP consists of four different pathways of radiative forcings and related GHG concentrations and emissions. The four pathways are denoted as RCP 8.5, 6.0, 4.5, and 3-PD (2.6), where the first three numbers represent stabilized radiative forcing in W m^{-2} after the year 2100, and the last value stands for 3-W m^{-2} peak and decline to 2.6 W m^{-2}.

Figure 7 shows changes in the $\Delta\bar{T}_s$ along the four pathways, defined as the anomaly relative to the value in the year 1990, and corresponding fractional changes in the δp_c and P_e with their uncertainties for RCP 6.0. For simplicity, $\Delta\bar{T}_s$ has been calculated by a simple climate model [40] using the equilibrium climate sensitivity of 3°C, which is defined as the global equilibrium surface warming after a doubling of the atmospheric CO_2 concentration. This simple calculation can be adapted to a more sophisticated formula to reflect advanced climate modeling and relevant uncertainties.

The difference in $\Delta\bar{T}_s$ among the four pathways increases from a negligible level during the first half of the 21st century to a spread of about 3°C in the year 2100. The results for the 1°C warming included in Table 1 correspond to changes expected around the year 2040 in any pathways, while those for the 2°C warming correspond to 2055, 2080, and 2100 for RCP 8.5, 6.0, and 4.5, respectively. The values for RCP 3-PD (2.6) are almost constant during the second half of the 21st century. However, it should be considered that such dating estimates strongly depend on climate sensitivity.

The upper and lower bounds of the RCP have been determined such that they cover existing emissions scenarios. It is understood from the comparison between the differences

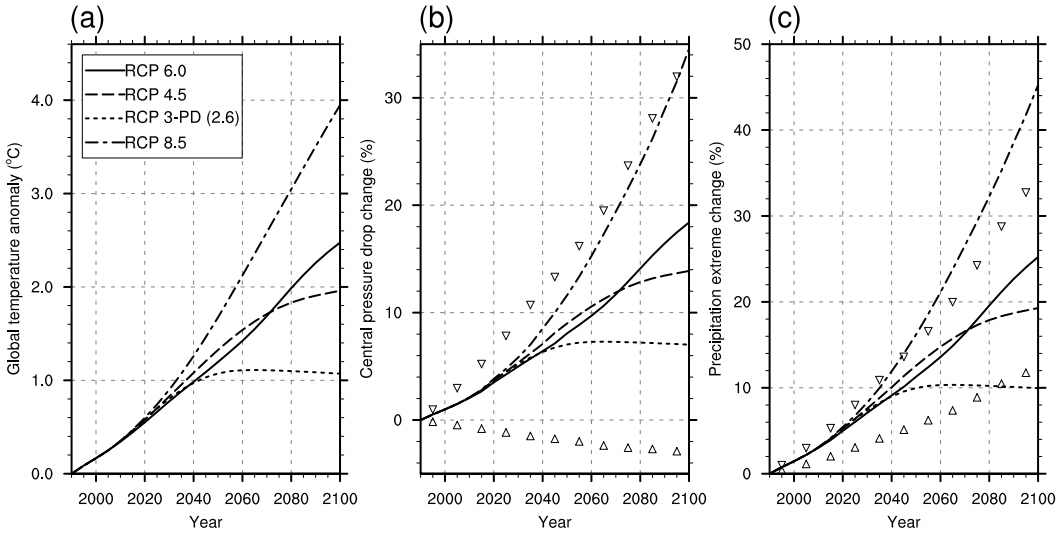

Figure 7. The global surface temperature anomaly $\Delta\bar{T}_s$ for the four pathways of the RCP (a), and corresponding fractional changes in the δp_c and P_e for Typhoon Flo just prior to landfall (b, c). The equilibrium climate sensitivity is assumed to be 3°C in computing $\Delta\bar{T}_s$. Markers in panels (b) and (c) indicate uncertainty ranges in the case of RCP 6.0. Source: Figure 3 of Reference [14].

among the pathways and the uncertainty ranges for a particular pathway (RCP 6.5 shown in the figure) that the uncertainty of the δp_c change is greater than the variation of possible future pathways. Although TC intensity is generally anticipated to be further intensified in warmed climates, the variation of the upper-air temperature anomalies in the current scientific understanding leads to a wide range of possibilities from virtually no change (or slightly negative) to double that of the best estimate. In contrast to the TC intensity measured by the δp_c, the uncertainty of the P_e change in 2100 is comparable to or smaller than the variation of the pathways. The increasing tendency of precipitation extremes is robust even if the large uncertainty of the TC intensity change is considered. The present scheme facilitates such a comparison of various uncertainties as in this example, which is particularly beneficial for determining priorities in adaptation planning.

4. Conclusion

This chapter describes a simple scheme for estimating changes in TC-caused strong winds and torrential rains resulting from GHG-induced warming on the basis of theoretical MPI and precipitation extremes. This scheme is designed for applications to risk assessment and policymaking associated with TC intensity in mitigation and adaptation strategies for warmed climates. For this purpose, changes in TC intensity measured by the central pressure drop δp_c at sea level and the precipitation extreme P_e representing a high percentile of precipitation rate are formulated as functions of the global surface temperature anomaly. Since the δp_c is related to the maximum wind speed and an idealized wind profile, changes

in the δp_c quantify changes in TC-caused strong winds and the dynamic effect of precipitation increase caused by warmed climates.

The present scheme is suitable for assessing changes anticipated in the future for a high-impact TC. An extremely strong TC rarely forms in the case of large fluctuations of natural climate variability, regardless of the background warming. It is generally difficult to assess relatively small background changes in the intensity of such a rare event by observation statistics or numerical climate projections. The present scheme overcomes this difficulty by focusing on background changes in large-scale thermodynamic conditions alone with no consideration of the dynamic conditions that dominantly control TC frequencies. Since disaster prevention programs and infrastructure design guides are, in many cases, developed on the basis of past high-impact TCs, assessment results for such TCs are beneficial for examination of these issues. Moreover, this scheme is expected to provide a quantitative physical basis, as documented in Reference [16, 41], for comparison of results from a large set of numerical experiments to improve understanding of TC activity in warmed climates.

As a case study in this chapter, Typhoon Flo in 1990 is considered a high-impact TC that produced excessive rainfall in Japan. When the global surface temperature rises by 1°C from the present, which is anticipated to occur around 2040, the δp_c and P_e observed just prior to Flo's landfall are projected to increase by 6.5% and 9.3%, respectively, and 5.6% in the case of P_e considering the thermodynamic effect alone. These values are the best estimates, based on the changes in the thermodynamic environment obtained from the CMIP3 AOGCMs. The variation in the AOGCMs of upper-air temperature anomalies has been used to quantify the uncertainty ranges of the intensity change and the dynamic effect of the precipitation change. Since the thermodynamic effect on increased precipitation due to climate warming is robust, the uncertainty range of the P_e change is relatively small. This assessment procedure is easily applied to arbitrary increases in global temperatures along various development pathways in the future, which facilitates comparison between various uncertainties relevant to development pathways and climate projections. With regard to the variation in the AOGCMs, the results presented in this chapter will be updated by the same procedure incorporating more advanced climate projections, which have been conducted for the next IPCC assessment report.

Although Flo is a typical high-impact event, increases in P_e should be further examined for many events because the degree of increase depends on the vertical structure of the updraft corresponding to the P_e. Moreover, the constraint on the vertical structure, which is assumed to be unaffected by the warming, should also be verified or relaxed to incorporate reliable tendencies, if available. This chapter has dealt with the maximum intensity and associated precipitation extreme alone. Additional aspects of TC activity should be addressed in the future in response to improved understanding of natural climate variations and continued advancement in climate modeling and projections.

Acknowledgment

The author acknowledges Dr. Masahiro Sugiyama of the Central Research Institute of Electric Power Industry for his valuable comments on precipitation extremes. The author also acknowledges the modeling groups, the Program for Climate Model Diagnosis and Intercomparison (PCMDI), and the World Climate Research Programme's (WCRP's) Working

Group on Coupled Modelling (WGCM) for their roles in providing the WCRP CMIP3 multi-model dataset. Support for this dataset is provided by the Office of Science, U.S. Department of Energy.

References

[1] IPCC WG1. *Climate change 2007: The physical science basis. Contribution of Working Group I to the fourth assessment report of the Intergovernmental Panel on Climate Change [S. Solomon, D. Qin, M. Manning, Z. Chen, M. Marquis, K. B. Averyt, M. Tignor and H. L. Miller (eds.)]*. Cambridge University Press, Cambridge (2007).

[2] K. A. Emanuel. *J. Atmos. Sci.*, **43**, 585 (1986).

[3] K. A. Emanuel. *J. Atmos. Sci.*, **52**, 3969 (1995).

[4] G. J. Holland. *J. Atmos. Sci.*, **54**, 2519 (1997).

[5] T. R. Knutson, J. L. McBride, J. Chan, K. Emanuel, G. Holland, C. Landsea, I. Held, J. P. Kossin, A. K. Srivastava and M. Sugi. *Nature Geoscience*, **3**, 157 (2010).

[6] J. C. L. Chan and K. S. Liu. *J. Climate*, **17**, 4590 (2004).

[7] G. A. Vecchi and B. J. Soden. *Nature*, **450**, 1066 (2007).

[8] S. Yokoi and Y. N. Takayabu. *J. Meteor. Soc. Japan*, **87**, 525 (2009).

[9] W. J. Merryfield. *J. Climate*, **19**, 4009 (2006).

[10] G. A. Vecchi, A. Clement and B. J. Soden. *EOS*, **89**, 81, 83 (2008).

[11] WMO. "Statement on tropical cyclones and climate change". Prepared by participants of the WMO International Workshop on Tropical Cyclones, IWTC-6, San Jose, Costa Rica, November 2006, available from `http://www.wmo.ch/web/arep/press_releases/2006/iwtc_summary.pdf` (2006).

[12] I. Grossmann and M. G. Morgan. *Clim. Change*. doi:10.1007/s10584-011-0020-1 (2011).

[13] J. Tsutsui. *J. Meteor. Soc. Japan*, **88**, 263 (2010).

[14] J. Tsutsui. *Journal of Japan Society of Civil Engineers, Ser. G (Environmental Research)*, **67**, I17 (2011). In Japanese.

[15] L. Chen. In R. L. Elsberry, editor, *Global perspectives on tropical cyclones*, WMO/TD-No. 693, TCP-38, chapter 6. World Meteorological Organization (1995).

[16] P. A. O'Gorman and T. Schneider. *Proc. Natl. Acad. Sci., USA*, **106**, 14773 (2009).

[17] R. Knutti and G. C. Hegerl. *Nature Geoscience*, **1**, 735 (2008).

[18] K. Onogi, J. Tsutsui, H. Koide, M. Sakamoto, S. Kobayashi, H. Hatsushika, T. Matsumoto, N. Yamazaki, H. Kamahori, K. Takahashi, S. Kadokura, K. Wada, K. Kato, R. Oyama, T. Ose, N. Mannoji and R. Taira. *J. Meteor. Soc. Japan*, **85**, 369 (2007).

[19] G. A. Meehl, C. Covey, T. Delworth, M. Latif, B. McAvaney, J. F. B. Mitchell, R. J. Stouffer and K. E. Taylor. *Bull. Amer. Meteor. Soc.*, **88**, 1383 (2007).

[20] M. G. Bosilovich, J. Chen, F. R. Robertson and R. F. Adler. *J. Appl. Meteor. Climatol.*, **47**, 2279 (2008).

[21] J. P. Camp and M. T. Montgomery. *Mon. Wea. Rev.*, **129**, 1704 (2001).

[22] R. K. Smith, M. T. Montgomery and S. Vogl. *Quart. J. Roy. Meteor. Soc.*, **134**, 551 (2008).

[23] K. A. Emanuel. *Nature*, **326**, 483 (1987).

[24] A. Henderson-Sellers, H. Zhang, G. Berz, K. Emanuel, W. Gray, C. Landsea, G. Holland, J. Lighthill, S.-L. Shieh, P. Webster and K. McGuffie. *Bull. Amer. Meteor. Soc.*, **79**, 19 (1998).

[25] T. R. Knutson and R. E. Tuleya. *J. Climate*, **17**, 3477 (2004).

[26] D. L. Hartmann. *Global Physical Climatology*. Academic Press (1994).

[27] J. R. Holton. *An introduction to dynamic meteorology*. Academic Press, 3rd edition (1992).

[28] G. D. Atkinson and C. R. Holliday. *Mon. Wea. Rev.*, **105**, 421 (1977).

[29] H. Koba, T. Hagiwara, S. Osano and S. Akashi. *Geophysical Magazine*, **44**, 15 (1991).

[30] H. E. Willoughby. In R. L. Elsberry, editor, *Global perspectives on tropical cyclones*, WMO/TD-No. 693, TCP-38, chapter 2. World Meteorological Organization (1995).

[31] R. W. Schloemer. "Analysis and synthesis of hurricane and wind patterns over Lake Okechobee, Florida". Hydrometeorological Report 31, U. S. Government Printing Office, No. C30.70:31 (1954).

[32] T. Fujii and Y. Mitsuta. *Annuals, Disaster Prevention Research Institute, Kyoto University*, **29, B-1**, 229 (1986). In Japanese.

[33] F. Fujibe and N. Kitabatake. *J. Meteor. Soc. Japan*, **85**, 747 (2007).

[34] R. L. Elsberry. *Bull. Amer. Meteor. Soc.*, **71**, 1305 (1990).

[35] T. Muramatsu. "A study on the changes of the three-dimensional structure and the movement speed of the typhoon through its life time". Technical Reports of the Meteorological Research Institute 14, Typhoon Research Division, Meteorological Research Institute, Japan (1985). In Japanese.

[36] N. Nakicenovic and R. Swart, editors. *Emissions scenarios. A special report of working group III of the Intergovernmental Panel on Climate Change*. Cambridge University Press, UK (2000).

[37] J. B. Elsner, J. P. Kossin and T. H. Jagger. *Nature*, **455**, 92 (2008).

[38] K. Oouchi, J. Yoshimura, H. Yoshimura, R. Mizuta, S. Kusunoki and A. Noda. *J. Meteor. Soc. Japan*, **84**, 259 (2006).

[39] R. Moss, M. Babiker, S. Brinkman, E. Calvo, T. Carter, J. Edmonds, I. Elgizouli, S. Emori, L. Erda, K. Hibbard, R. Jones, M. Kainuma, J. Kelleher, J. F. Lamarque, M. Manning, B. Matthews, J. Meehl, L. Meyer, J. Mitchell, N. Nakicenovic, B. O'Neill, R. Pichs, K. Riahi, S. Rose, P. Runci, R. Stouffer, D. van Vuuren, J. Weyant, T. Wilbanks, J. P. van Ypersele and M. Zurek. *Towards new scenarios for analysis of emissions, climate change, impacts, and response strategies*. Intergovernmental Panel on Climate Change, Geneva (2008).

[40] J. Tsutsui. *Journal of Japan Society of Civil Engineers, Ser. G (Environmental Research)*, **67**, 134 (2011).

[41] M. Sugiyama, H. Shiogama and S. Emori. *Proc. Natl. Acad. Sci., USA*, **107**, 571 (2010).